

Supporting Information : Understanding the nanoscale structure of hexagonal phase lyotropic liquid crystal membranes

Benjamin J. Coscia Douglas L. Gin Richard D. Noble Joe Yelk Matthew Glaser

Xunda Feng Michael R. Shirts

E-mail:

1 Attempted Self-assembly

We attempted self assembly of Na-GA3C11 monomers by using an isotropic configuration generated using Packmol⁷ (Figure 1a). The input file given to Packmol is shown below.

```
tolerance 2.0
output packed.pdb
filetype pdb
structure monomer.pdb
number 400
inside box 0. 0. 0. 84.3 84.3 84.3
end structure
```

We used the same number of monomers (400) that we used in all other simulations. Since Packmol does not have the capability to create monoclinic boxes, we used a cubic box with a volume of 660 nm^3 , 25 % larger than those used to create ordered unit cells we studied. We tested systems with semiisotropic and anisotropic pressure coupling since the shape of the unit cell will likely need to change in order to accomodate hexagonally packed pores.

We use the nematic order parameter as defined in section 5 to observe any progress towards system ordering. In both cases, we see that the nematic order parameter stays close to zero for the duration of the simulation time, indicating an isotropic arrangement of head groups (Figure 1b). The values are slightly negative since there are only 400 monomers. Equation 2 is bounded between -1 and 1, however, with a proper choice of nematic director, measured values will range between 0 and 1. With a large number of samples, an isotropic system would have an order parameter of 0.

2 Further details regarding monomer parameterization

We parameterized monomers according to the following procedure:

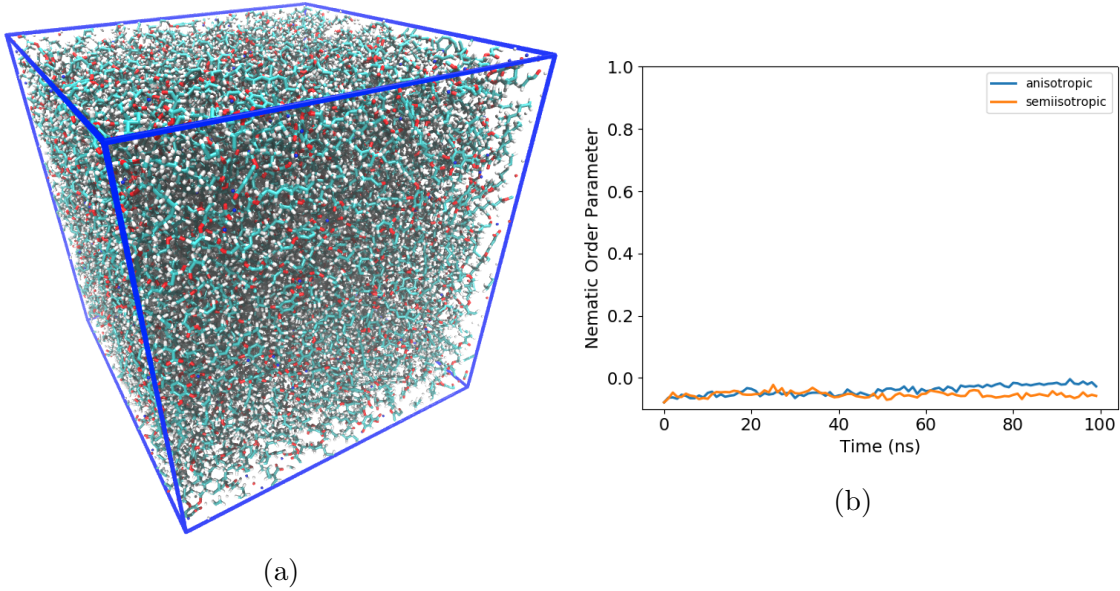


Figure 1: (a) We created a box of isotropically packed monomers and allowed it to simulate for 100 ns using isotropic and anisotropic pressure coupling. (b) The nematic order parameter hovers close to zero for the duration of the simulation meaning the system maintains its isotropic alignment.

1. *Create monomer structure file with connectivity* : We drew atomistic structures using MarvinSketch 17.13[?] with all hydrogen atoms drawn out explicitly. We optimized the 3D geometry of the structure using the 'Clean in 3D' function of MarvinSketch. We saved the structure as a .mol file, then converted it to .pdb format using Open Babel 2.4.1.^{??}
2. *Assign GAFF atomtypes using antechamber* : Using the .pdb structure file as input, we ran `antechamber`[?] using the AM1-BCC charge model. The net charge on the monomer is input as -1 since the sodium ion is kept as a separate residue. We use LEaP[?] and the output of `antechamber` to create Amber topology files. A detailed tutorial can be accessed elsewhere.[?]
3. *Create GROMACS topologies from Amber output* : The output of LEaP is a .inpcrd and a .prmtop file which are Amber topology files. Using acpype.py,[?] we converted the LEaP output into GROMACS .gro and .top files.

4. *Perform a simulated annealing procedure on the monomer* : We created a cubic box around the monomer using the GROMACS command `gmx editconf`. The monomer was centered in the box with edges of the box spaced at least 3 nm from the monomer on all sides. We ran an energy minimization on the system with the steepest descent algorithm. Next we performed an NVT simulated annealing procedure. We linearly decreased the temperature of the system from 1000 K to 50 K over the course of 10 ns. We randomly chose a monomer configuration from the last 10 % of the trajectory.
5. *Reassign charges with molcharge*: With the monomer configuration taken from the annealed trajectory, we reassigned charges using `molcharge` with the am1bccsym method in order to ensure charges are symmetric. This condition is not guaranteed with `antechamber`. The charges in the GROMACS topology file (.top) were replaced with the new charges calculated by `molcharge`.
6. *Anneal again to get final structure* : We repeated the same simulated annealing procedure using the monomer topology with `molcharge` charges. A random monomer configuration was pulled from the last 10 % of the trajectory and was used to build all assemblies reported (Figure 2).

3 Calculation of pore-to-pore spacing statistics

We are interested in 5 pore-to-pore distances which should all be equal in a perfect hexagonal array (Figure 11). Only 4 of the 5 distances are independent. We can calculate a trajectory of spacing versus time for each of the 5 distances. We calculated the average pore-to-pore spacing and its uncertainty according to the following procedure:

1. We calculated the time when each of the pore-to-pore distances were equilibrated using `pymbar.timeseries.detectEquilibration()`? ? We began calculations after the largest of the five values.

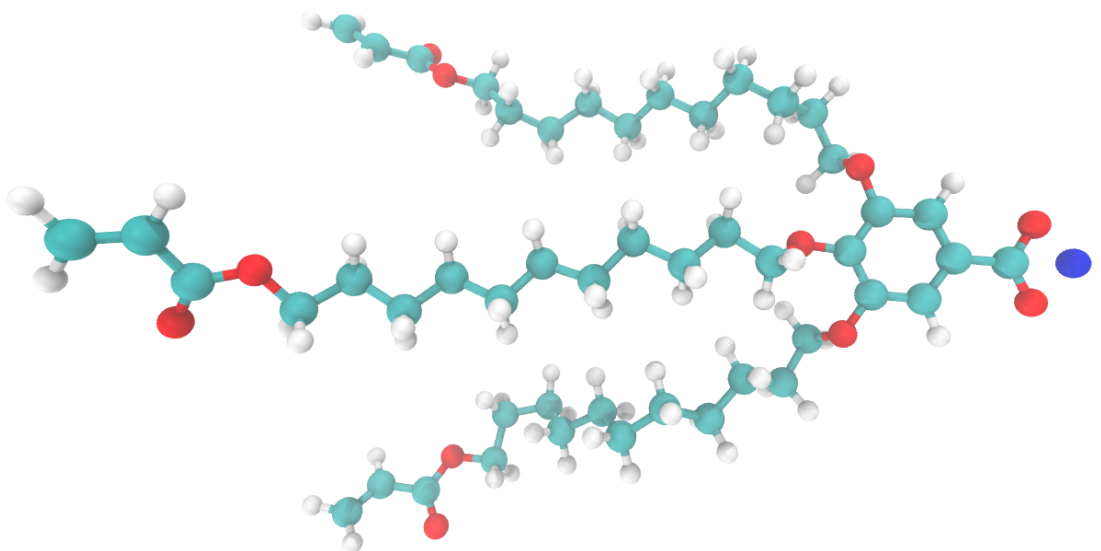


Figure 2: Atomistic representation of the monomer Na-GA3C11. White atoms represent hydrogen, cyan atoms represent carbon, red atoms represent oxygen and the blue atom is sodium.

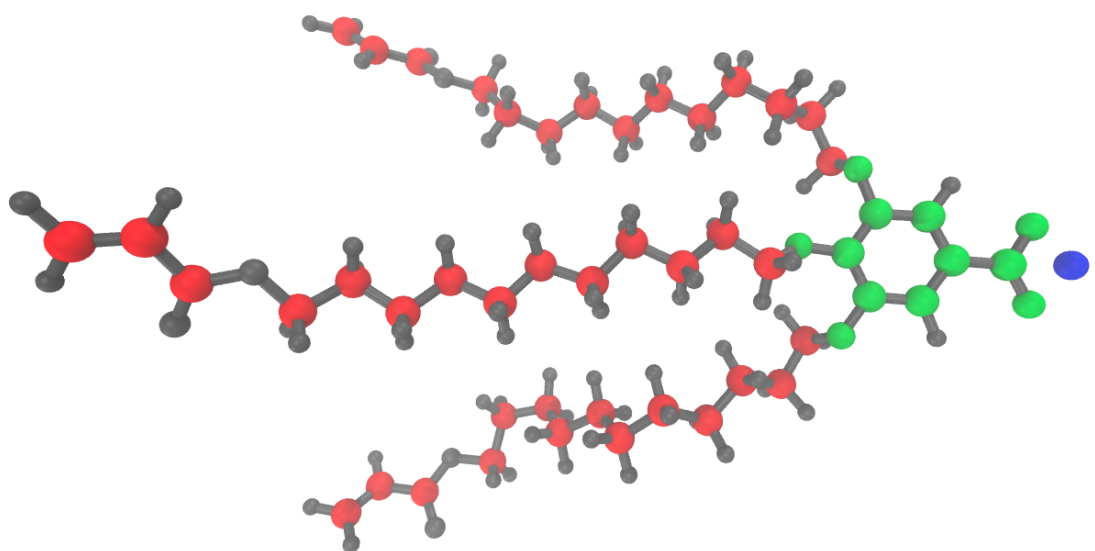


Figure 3: The groups used for radial distribution calculations. Red atoms are in the tails group. Green atoms are in the head group region. The blue atom is sodium.

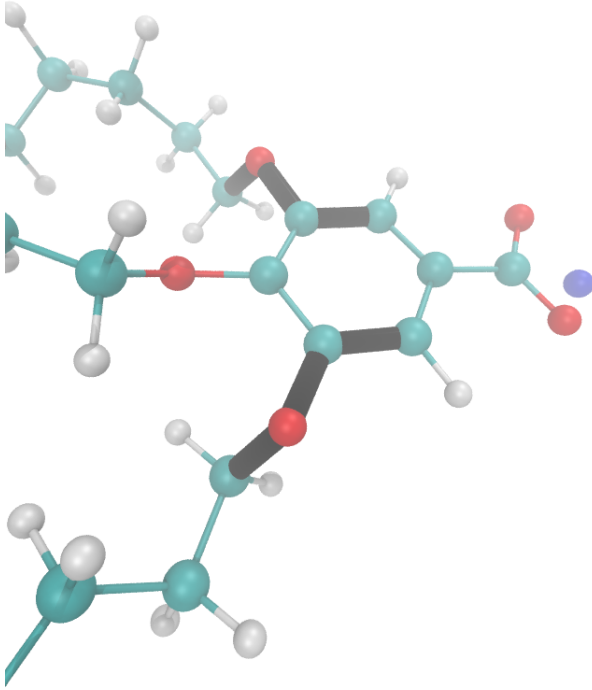


Figure 4: We measured the autocorrelation functions of the dihedrals highlighted in black. We only included dihedrals associated with the outer tails in our calculation since the position of the center tail leads to fundamentally different interactions and dynamics.

2. We calculated how long it takes for the data in each of the 5 trajectories to become uncorrelated using `pymbar.timeseries.integratedAutocorrelationTime()`.^{??}
3. We broke the full equilibrated trajectory into blocks of length τ , where τ is the maximum of the five autocorrelation times calculated. Each block contains five sub-trajectories of pore-to-pore spacings.
4. We generate statistics using the bootstrapping technique. For each bootstrap trial, we reconstruct an equilibrium trajectory by randomly sampling from the trajectory blocks.
5. The average pore-to-pore distance is the mean of all pore spacings among all bootstrap trials.
6. To calculate the uncertainty in pore-to-pore distance, we calculate the average pore

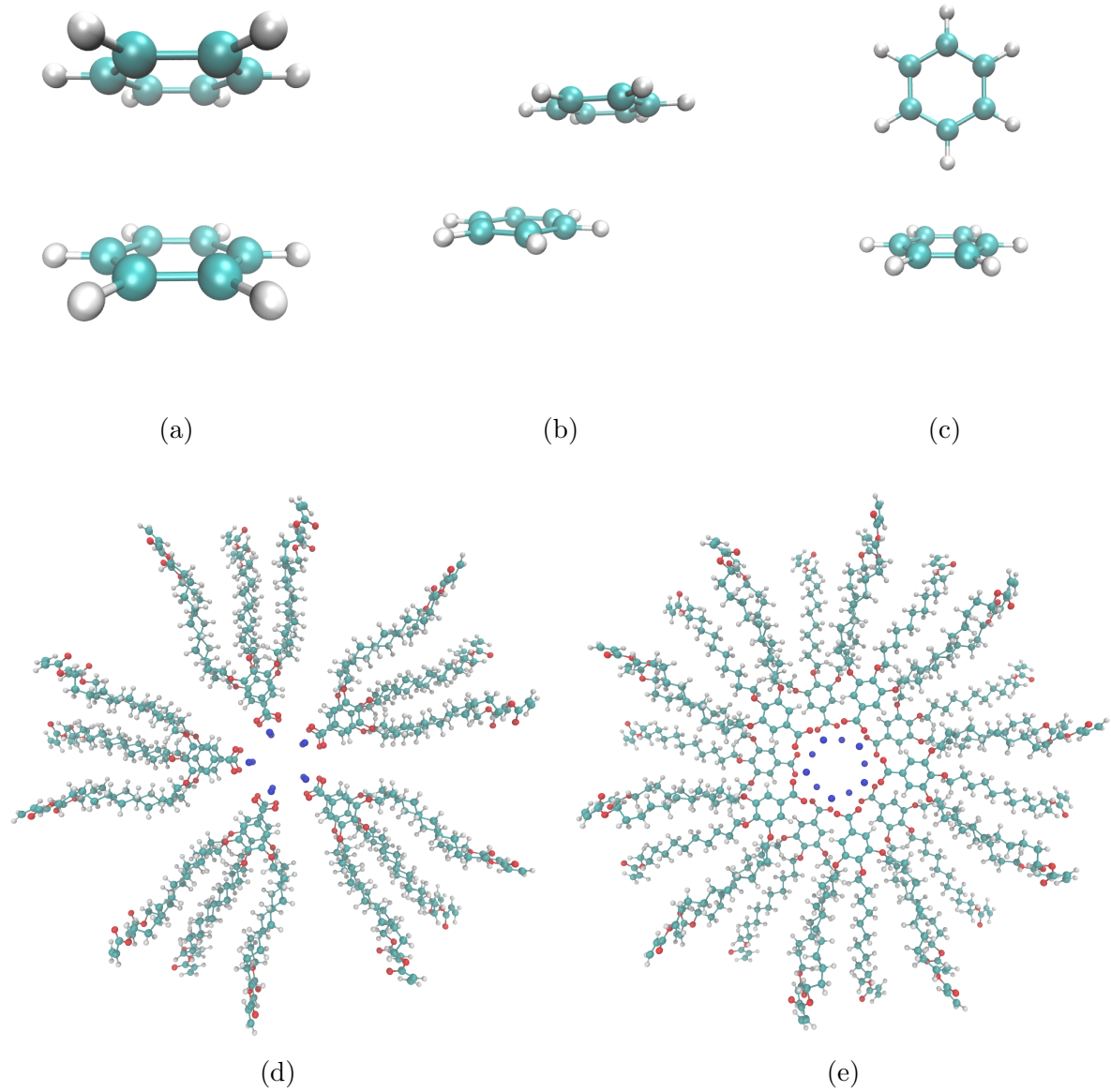


Figure 5: (a) Sandwiched benzene dimers stack 3.8 Å apart. (b) Parallel-Displaced benzene dimers stack 3.4 Å vertically and 1.6 Å horizontally apart. (c) T-shaped benzene dimers stack 5.0 Å apart. (d) Two monomer layers stacked in the sandwiched configuration (e) Two monomer layers stacked in the parallel-displaced configuration

spacing for each pore over all bootstrap trials. Using the 5 average pore-to-pore distances, we calculate the spread with:

$$s = \sqrt{\frac{1}{4} \sum_{i=1}^5 (x_i - \bar{x})^2} \quad (1)$$

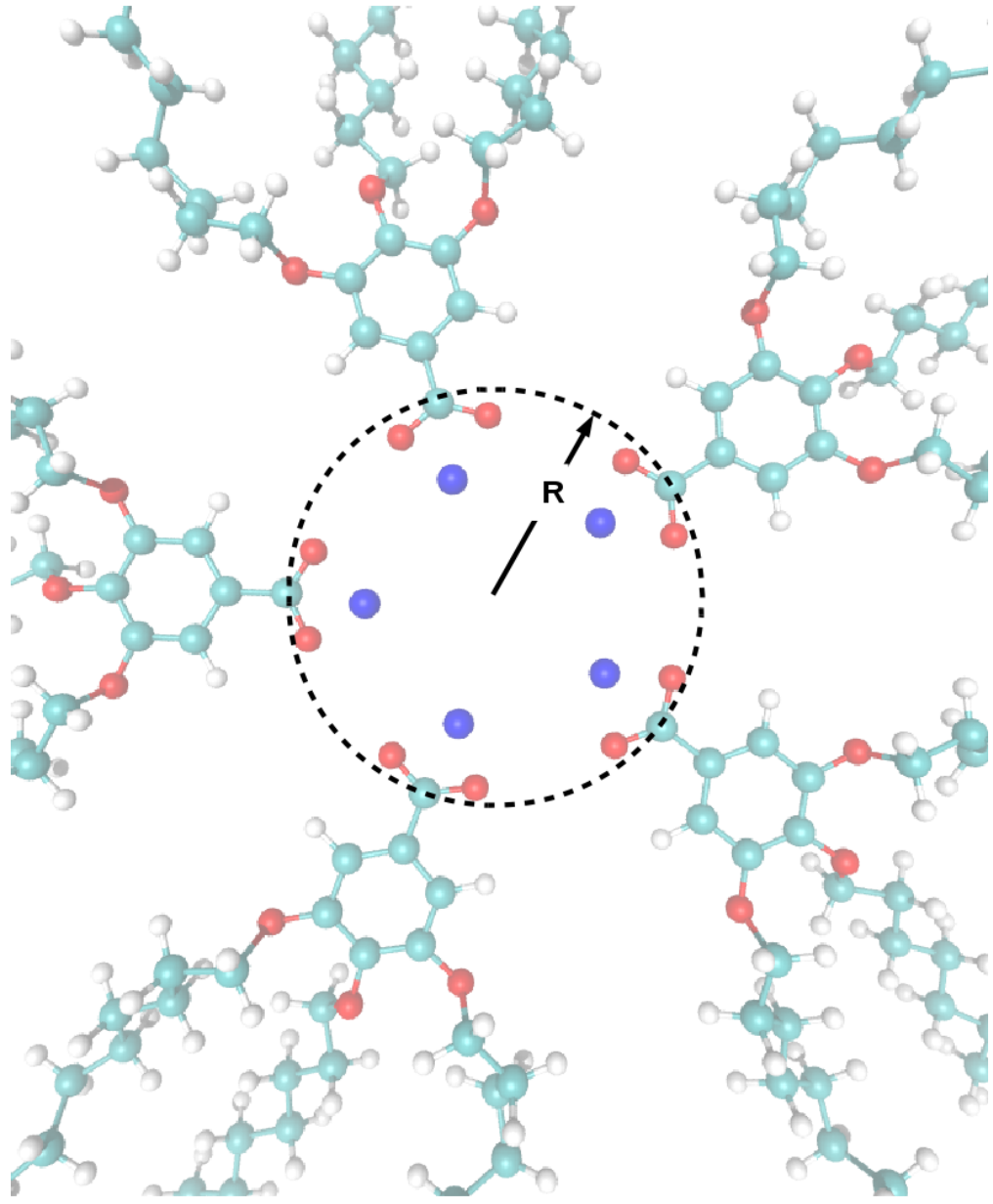


Figure 6: When creating an initial configuration, the pore radius is defined based on the distance of the carbonyl carbon from the pore's central axis

where \bar{x} is the average pore-to-pore distance. We divided the sum in equation 1 by 4 since there are only 4 independent pore spacings.

4 Initial Configuration Dependence

We addressed any major dependence on initial configuration in the main text. There we showed that systems are stable when made with 4, 5, 6, 7, and 8 monomers per layer. We also showed that systems are stable when monomer head groups are oriented in the parallel displaced and sandwiched configurations (See Figure 5). Our model is most consistent with experiment when built with 5 monomers per layer, with layers stacked 3.7 Å apart in the parallel displaced configuration.

There are three other parameters whose choice may influence the equilibrium structure: initial pore spacing, initial pore radius and initial distance between layers. Here we show the results of a sensitivity analysis performed on the three parameters. To reduce the size of the sensitivity analysis, we only tested systems built with 5 monomers per layer with layers stacked in the parallel displaced configuration. We equilibrated all systems according to the dry equilibration procedure.

4.1 Initial pore spacing

We tested five different initial pore spacings, defined as the distance between the central axis of each pore with all others (Figure 11). To reduce the number of variables, we held the pore radius constant, at 6 Å and the distance between layers at 3.7 Å since those were the values used in our optimal system in the main text. We prioritized ensuring that resulting configurations maintain the expected hexagonal symmetry. If initial pore spacing is too small, we observe repulsion between columns which disrupts equilibration. If the pore spacing is too large the pores squeeze together, but in a distorted hexagonal array because the xy initial translation of the pores is somewhat erratic.

1. 39 Å : We tested a pore spacing of 39 Å in order to have a test system with an intial spacing below the experimental value. As soon as the restraining potential switches

to 56 KJ mol⁻¹ nm⁻², the columns are able to repel resulting in a large jump in pore spacing (Figure 8a).

2. 41 Å : We chose to test a pore spacing of 41 Å since it closely matches the experimental pore spacing. Again, we observe abrupt repulsion of columns once the restraining potential is switched to 56 KJ mol⁻¹ nm⁻² (Figure 8b).
3. 45 Å : A pore spacing of 45 Å is about 10 % larger than the experimental value. This systems exhibits the smallest response to our equilibration procedure (Figure 8c) and we chose to use this value for all our simulations in the main text.
4. 50 Å : We tested a pore spacing of 50 Å, about 20 % larger than the experimental value. Once the restraining potential reaches 56 KJ mol⁻¹ nm⁻², the pore spacing begins to decrease rapidly, following a linear trend (Figure 8d).
5. 55 Å : We tested a pore spacing of 55 Å which is at a distance where monomers in each pore no longer intersect those of adjacent pores. Once the restraining potential reaches 56 KJ mol⁻¹ nm⁻², the pore spacing changes erratically until it begins to settle when the force constants are below 3 KJ mol⁻¹ nm⁻² (Figure 8e). We reccomend avoiding a system such as this where vacuum gaps between pore columns are introduced unnecessarily.

4.2 Initial pore radius

We tested 3 different pore radii, defined as shown in Figure 6. For each system, we held the initial pore spacing constant at 45 Å and the initial distance between layers constant at 3.7 Å. Equilibrated values of pore radii are presented in Table 1. The pore radius in each simulation frame is calculated as the average distance of all carbonyl carbons (See Figure 6) from their associated pore center. Statistics for the pore radii reported were generated from the timeseries representing the average pore radius at each frame. We detected equilibration

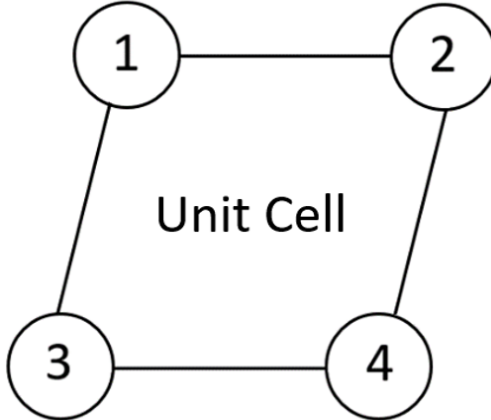


Figure 7: In a perfect hexagonal, there are 5 distances that should be exactly equal. As pictured in this diagram the distance from 1-2, 1-3, 1-4, 2-4, and 3-4 are the same.

using `pymbar.timeseries.detectEquilibration`. We calculated the average and standard deviation of pore radii using only data points collected after equilibration was detected.

1. 2.5 Å : The smallest pore radius that we can achieve before energy minimization becomes problematic is 2.5 Å. After being run through the full dry equilibration procedure, the average pore radius is 0.40 ± 0.01 Å.
2. 5 Å : We tested a pore radius of 5 Å because it is slightly larger than the equilibrated pore radius of the system simulated with an initial pore radius of 2.5 Å. After being run through the full dry equilibration procedure, the average pore radius is 0.42 ± 0.01 Å, which agrees with the 2.5 Å configuration within uncertainty.
3. 8 Å : The largest pore radius that can be achieved before energy minimization becomes problematic is 8 Å. One should use caution with such a structure because of the relatively large vacuum space that is created in the pore region of the initial configuration. After being run through the full dry equilibration procedure, we see a combination of cylindrical and slit-like pores (Figure 9). Measuring the pore radius of this system does not have a concrete meaning since slits do not have a single radius, but its calculated value is reported in Table 1. We are wary of such a non-symmetric structure and choose not to use a pore radius of 8 Å for our starting configurations.

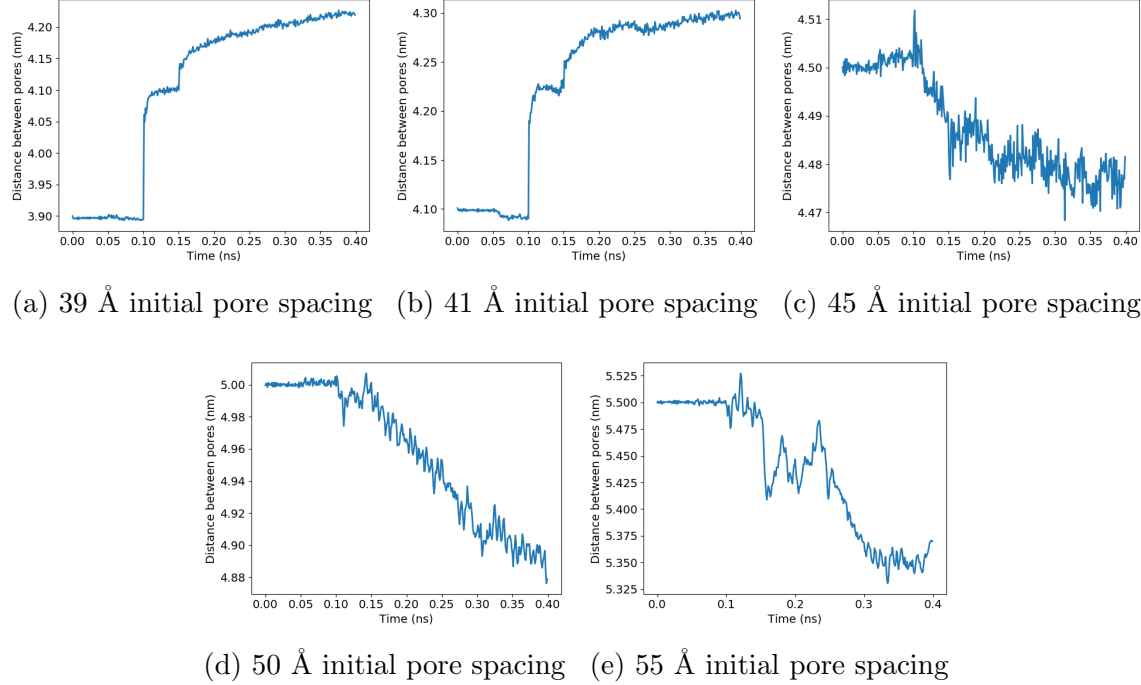


Figure 8: The pore spacing during the restrained portion of the dry equilibration procedure is shown. Every 50 ps (0.05 ns) position restraints are reduced according to the sequence: 1000000, 3162, 56, 8, 3, 2, 1, 0 KJ mol⁻¹ nm⁻². When the initial pore spacing is chosen below the experimental value (a) or at the experimental value (b), there is an abrupt change in pore spacing when the position restraints are reduced to 56 KJ mol⁻¹ nm⁻². When pores are started 45 Å apart (c) the pore spacing remains relatively stable. When pores are spaced 50 Å apart (d), the pore spacing decreases nearly linearly once the restraints are reduced to 56 KJ mol⁻¹ nm⁻². When pores are spaced 55 Å apart (e), so that monomers do not intersect with adjacent pores, and position restraints are reduced to 56 KJ mol⁻¹ nm⁻², the pore spacing changes erratically before stabilizing when force constants are reduced below 3 KJ mol⁻¹ nm⁻².

4.3 Initial distance between layers

We tested 3 different initial layer spacings, defined as the distance between the planes of aromatic rings in each layer. Systems built with layers stacked 3.7 Å and 5 Å apart are discussed extensively in the main text. We also tested a system built with layers stacked 10 Å apart.

Figure 10 shows the structure of an assembly built with an initial layer spacing of 10 Å immediately after the restrained portion of the equilibration procedure. Since we used position restraints, the simulations were run in the NVT ensemble. When layer spacing is

Table 1: The average pore radii of systems built with an initial pore radius of 2.5 Å and 5 Å equilibrate to values that agree within error. If the pore radius is too large, slit pores may form.

Initial Pore Radius	Equilibrated Pore Radius
2.5 Å	0.40 ± 0.01 Å
5 Å	0.42 ± 0.01 Å
8 Å	0.69 ± 0.01 Å

large, such as this situation, there is a significant amount of vacuum space which the monomer attempts to fill. Even if turning pressure control on allows the system to recover the geometry of the hexagonal phase, we would likely need much longer equilibration times, and it will almost certainly get trapped in a metastable configuration that bears no resemblance to the experimental profile.

5 The nematic order parameter

We calculated the nematic order parameter for our system in order to understand the degree of ordering among monomer head groups. Typically, the nematic order parameter is calculated for nematic liquid crystal systems which are characterized by unidirectional ordering of liquid crystal monomers. The preferred direction of monomers is defined by the unit director vector, \mathbf{n} . Assuming a single preferred direction of alignment, the nematic order parameter, S , is defined as:

$$S = \frac{1}{2} \langle (3 \cos^2 \theta - 1) \rangle \quad (2)$$

where θ is the angle between the molecular long axis and \mathbf{n} . In a perfectly ordered nematic liquid crystal system, the molecular axis of each monomer should be aligned with \mathbf{n} and give an order parameter of $S = 1$. We are interested in quantifying the degree of monomer head group alignment between systems. We use Eq. 2 to accomplish this by defining \mathbf{n} as the z-axis (or pore axis), and then measuring the angles, θ , between \mathbf{n} and the vectors perpendicular to the plane of the aromatic head groups (\mathbf{v} in Figure 12).

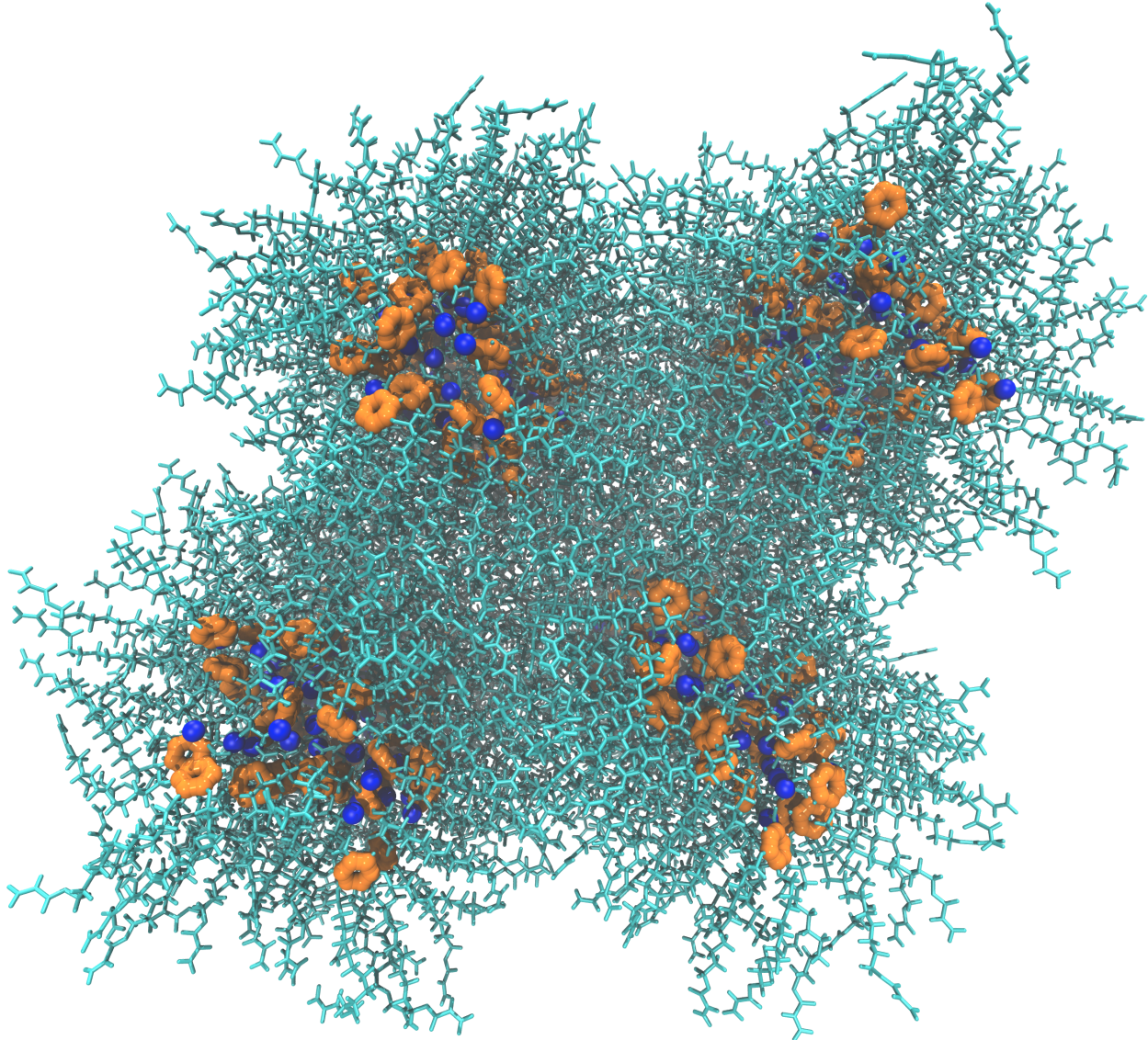


Figure 9: A system that was built with an initial pore radius of 8 Å equilibrates to a structure that exhibits both cylindrical and slit-like pores. As pictured here, sodium ions are colored blue, carbon atoms in the aromatic ring of the head group are colored orange and all else is colored cyan.

The nematic order parameter is highest in sandwiched systems. Figure 13 shows the distribution of angles between the nematic director and the vector perpendicular to the monomer head groups. Systems in the ordered basin have higher nematic order parameters than their disordered basin counterparts. Both sandwiched system have higher nematic order parameters than both parallel displaced systems. This may occur because monomers in the

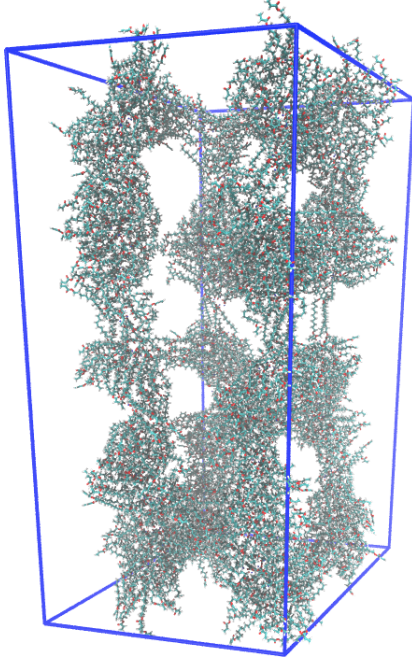


Figure 10: When layers are initially stacked 10 Å apart and the system is equilibrated using the dry equilibration procedure, large vacuum gaps form as the monomers attempt to fill space.

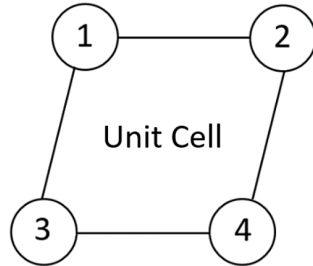


Figure 11: There are five pore-to-pore distances that are equal in a perfect hexagon. If each number in the diagram represents the center of a pore in a hexagonal unit cell, then the distance from 1 to 2, 2 to 4, 4 to 3, 3 to 1 and 1 to 4 should be equal. Only 4 of the distances are independent. For example, the distance from 1 to 4 is defined by the location of all other pore centers.

sandwiched configuration have their motion restricted by vertically adjacent monomers, while those in the parallel displaced configuration have more room to rotate.

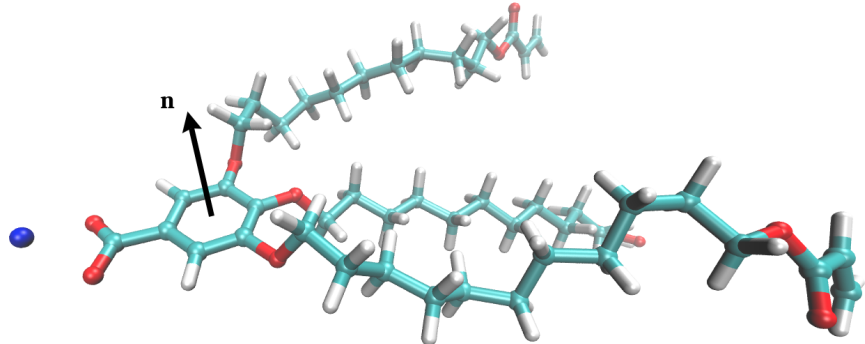


Figure 12: We calculate the nematic order parameter by measuring the angle between \mathbf{v} and the z-axis.

6 Measurement of intensities of experimental and simulated XRD patterns

We developed standardized methods of measuring the intensity of reflections of interest in the experimental and simulated X-ray diffraction patterns presented in this work. Here, we graphically illustrate the methods used for measuring these intensities.

All diffraction patterns are normalized according to R-alkanes and the intensities of all reflections are reported relative to the intensity of R-alkanes. The region used to calculate the average intensity of R-alkanes is shown in Figure 14b. The top region is excluded because, in the simulated patterns, R- π intersects with R-alkanes.

R- π and R-double are reported as the maximum values of the peaks of the q_z cross-section of the experimental pattern at $q_r = 0$ (Figure 14c). In the case of the experimental pattern, the peak heights are not symmetrical, so we report the average of the two heights.

We measured R-spots by calculating the average intensity within a region selected by visual inspection. We report the average intensity within the regions highlighted in red in Figure 14d. If there are no easily discernable spots, we report the average intensity at the intersection of R-alkanes with the q_z value of R-double since that is where we expect it to

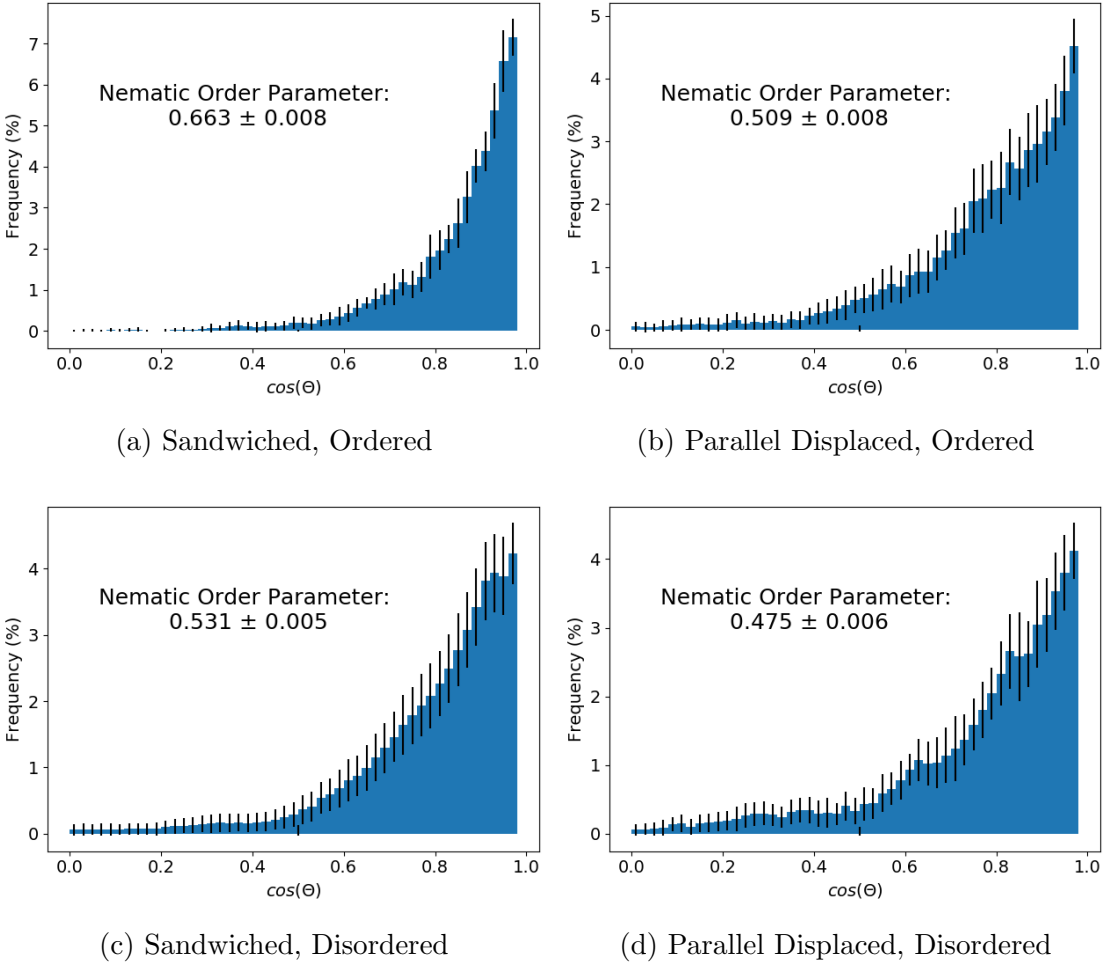


Figure 13: The distribution of angles between nematic director vector (See Figure 12) and the z-axis averaged over the equilibrated portion of each trajectory

appear based on experiment. Since R-double does not appear in our simulated patterns, we estimate where it should appear as half of the q_z value of R- π .

7 Noise in simulated diffraction patterns

The magnitude of noise in the simulated diffraction patterns decrease as the number of independent configurations increases. We simulated the structure factor of 100 randomly placed particles and varied the number of independent configurations (N). It is expected that the structure factor should resemble a two-dimsional gaussian. We cannot sample

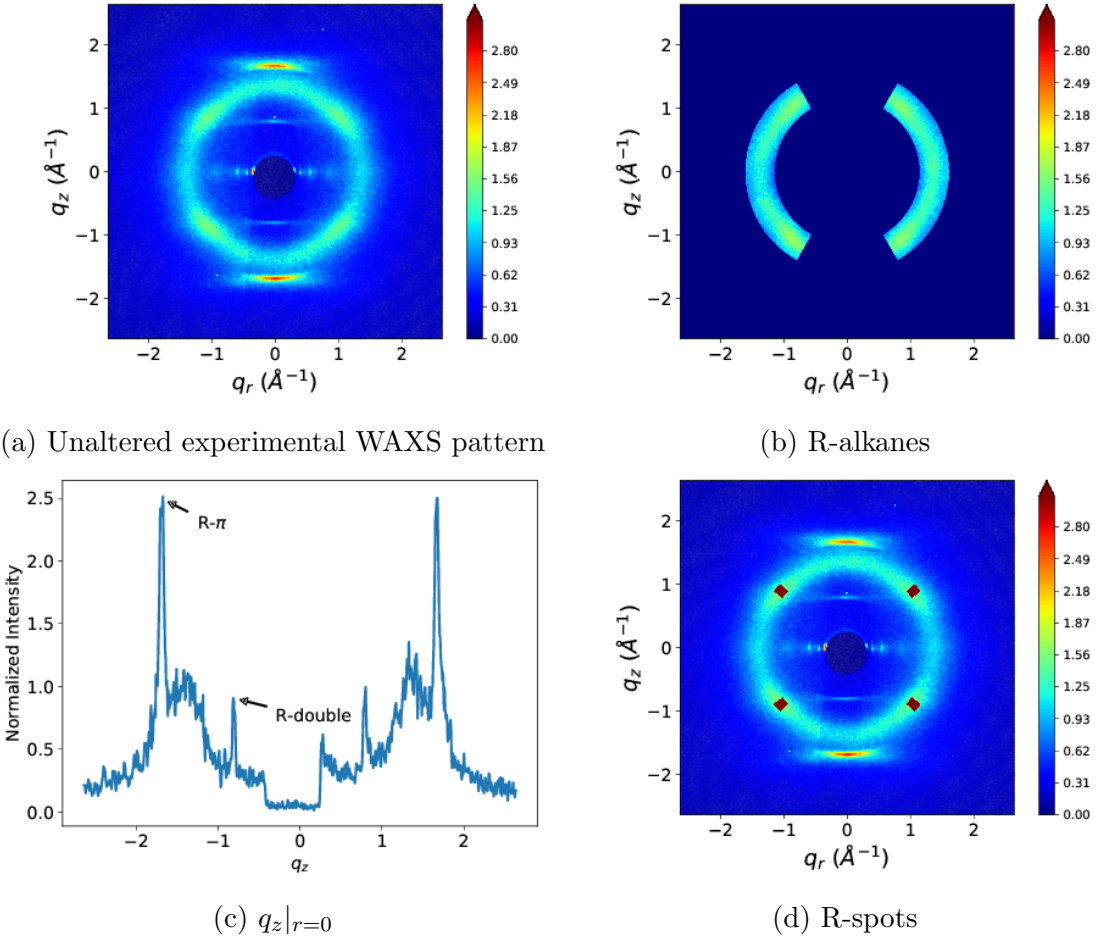


Figure 14

enough independent configurations of our system to completely eliminate noise.

8 Experimental correlation length of R- π

Experimentalists did not measure the correlation length, so we estimated it from the raw data. We took a slice of the 2D WAXS data along the dashed line in Figure 16a. We removed background noise by subtracting the intensity far from the pattern (high q) uniformly. We used a least squares algorithm to fit a lorentzian curve to the data. Only values recorded above $q_z = 1.6$ were considered for the fit in order to mitigate interference from R-alkanes (Figure 16b). The full width at half maximum (FWHM) is related to the correlation length,

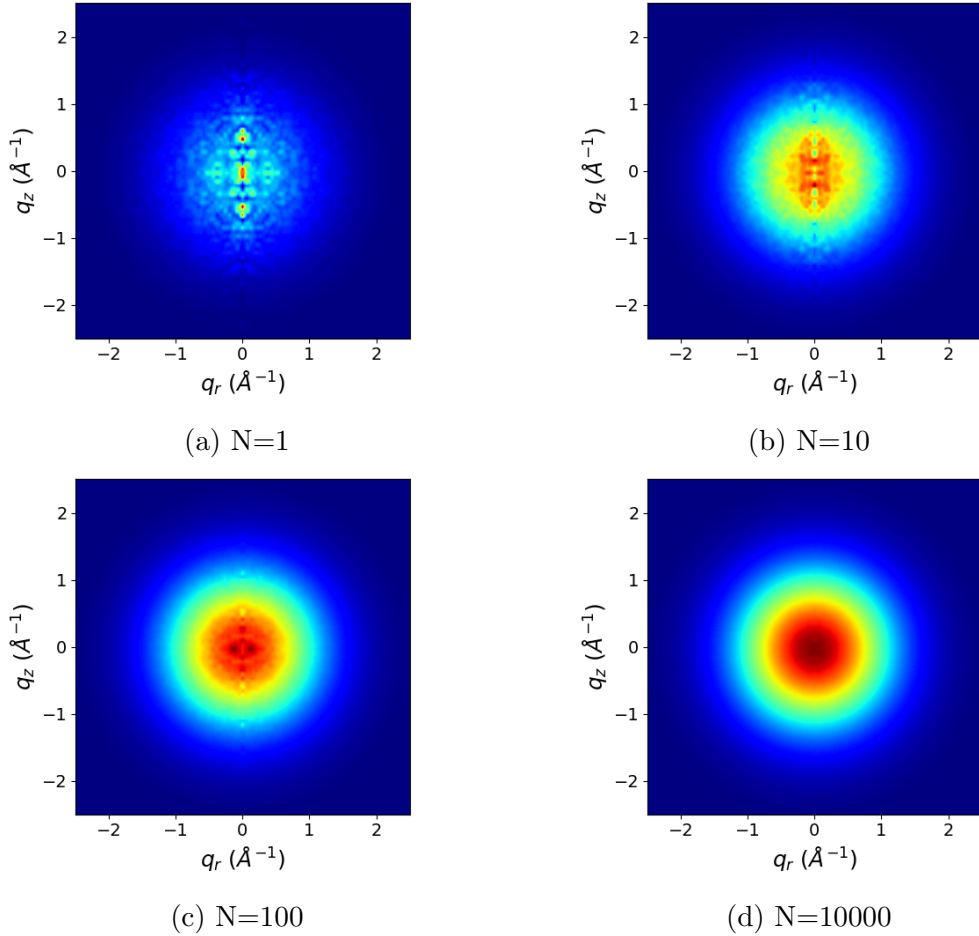


Figure 15: The magnitude of noise, especially along $q_r=0$, decreases as the number of independent configurations (N) increases.

L , by the relationship: $L = \frac{1}{FWHM}$. The error in the value is calculated as the square root of the diagonal entry of the covariance matrix of optimized fit parameters. We estimate the value of the correlation length to be 10 ± 1 using this method. Since the experimental peak width is also influenced by strain and instrumental broadening in addition to finite size broadening, the value calculated here is really only an upper bound on the correlation length.

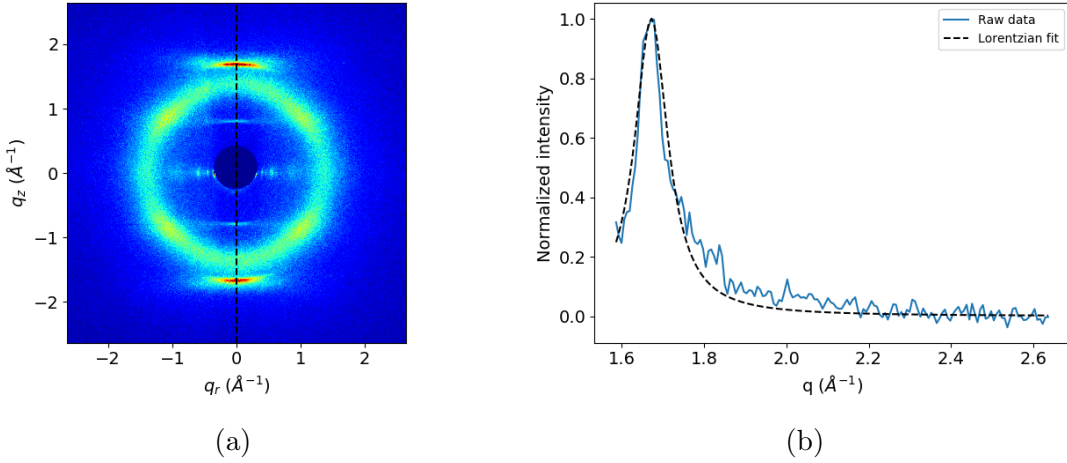


Figure 16: (a) We estimated the system’s experimental correlation length using a 1D slice of the 2D WAXS patterns along $q_r=0$. (b) We fit a lorentzian curve to the 1D slice. One of the fit parameters is the full width at half maximum (FWHM). The correlation length is $1/\text{FWHM}$.

Table 2: The diffusion constants for all systems are on the order of $10^{-14} m^2/s$ which is three orders of magnitude lower than literature values.

System	Diffusion Constant (m^2/s)
Sandwiched, Ordered	1.4e-14
Parallel Displaced, Ordered	2.0e-14
Sandwiched, Disordered	2.0e-14
Parallel Displaced, Disordered	3.5e-14

9 Demonstrative fourier transforms

Here we use Fourier transforms to demonstrate some of the arguments made in the main text. Interpretation of real and simulated X-ray diffraction patterns is non-trivial and requires careful thought. They are a function of the positions of all atoms in space, and suffer from the phase problem. Namely, there are multiple solutions that could explain a single diffraction pattern. Using simplified models, we can hypothesize about the effect of various configurations on the simulated patterns.

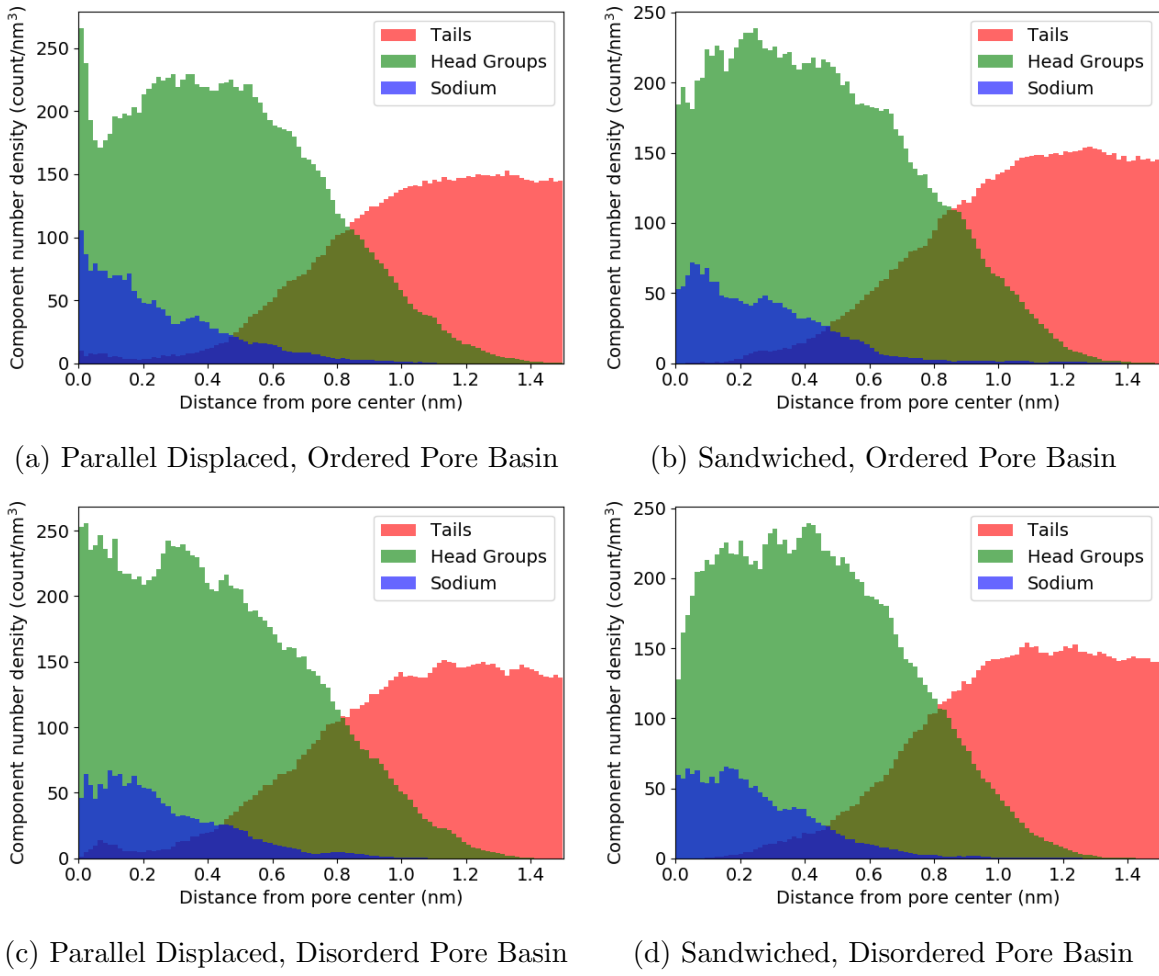


Figure 17: In all cases, the component radial distribution functions exhibit a composition gradient transitioning from the hydrophilic to the hydrophobic regions. Systems with layers initially spaced 3.7 Å apart in the parallel displaced (a), and sandwiched (b) configurations both show the highest concentrations of ions and head groups away from the pore center. Systems with layers initially spaced 5 Å apart (c) and (d), both show the highest concentrations of ions and head groups near the pore center, implying a more uniform, disordered pore.

9.1 Magnitude of $\mathbf{R}\cdot\boldsymbol{\pi}$

In all cases, the magnitude of $\mathbf{R}\cdot\boldsymbol{\pi}$ in our system is larger than that in experiment. Some of the discrepancy can be explained by defects and imperfect pore alignment. However, there are significant effects resulting from the ordered states that we simulate.

Persistent oscillations in the z-correlation function, $g(z)$, increase the intensity of $\mathbf{R}\cdot\boldsymbol{\pi}$.

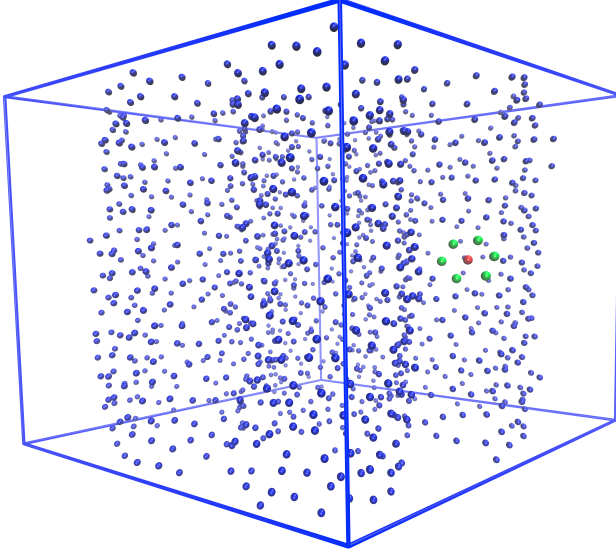


Figure 18: Monomer tails pack together hexagonally. The centroid of each tail is visualized as a blue sphere. The centroids are calculated based on the red atoms in Figure 3. The red sphere highlights an example of an alkane tail centroid with its nearest neighbors (green spheres) surrounding it in a hexagonal pattern.

In Figure 21a, we fit a decaying sinusoidal function (equation 3 of the main text) to $g(z)$ calculated from the sandwiched configuration in the ordered basin. While the sinusoidal decay fit decays to one rather quickly, $g(z)$ continues to oscillate with nearly the same amplitude as its third peak. In Figure 21b, we overlay the same decaying sinusoidal fit with a function that continues to oscillate with the same amplitude as the third peak of the fit to $g(z)$. In Figure 21c, we plot the power spectrum generated from the discrete Fourier transform of the plots in Figure 21b. The maximum intensity of the power spectrum increases by nearly 60 % when the correlation function does not decay to one. This explains, in part, the large simulated value of the intensity of R- π .

9.2 Simplified assemblies

We explored the sandwiched and parallel displaced configurations as potential ways for aromatic head groups to stack. We used copies of the same monomer to build each system. We were unable to create any assemblies which exhibited R-double using this technique. We

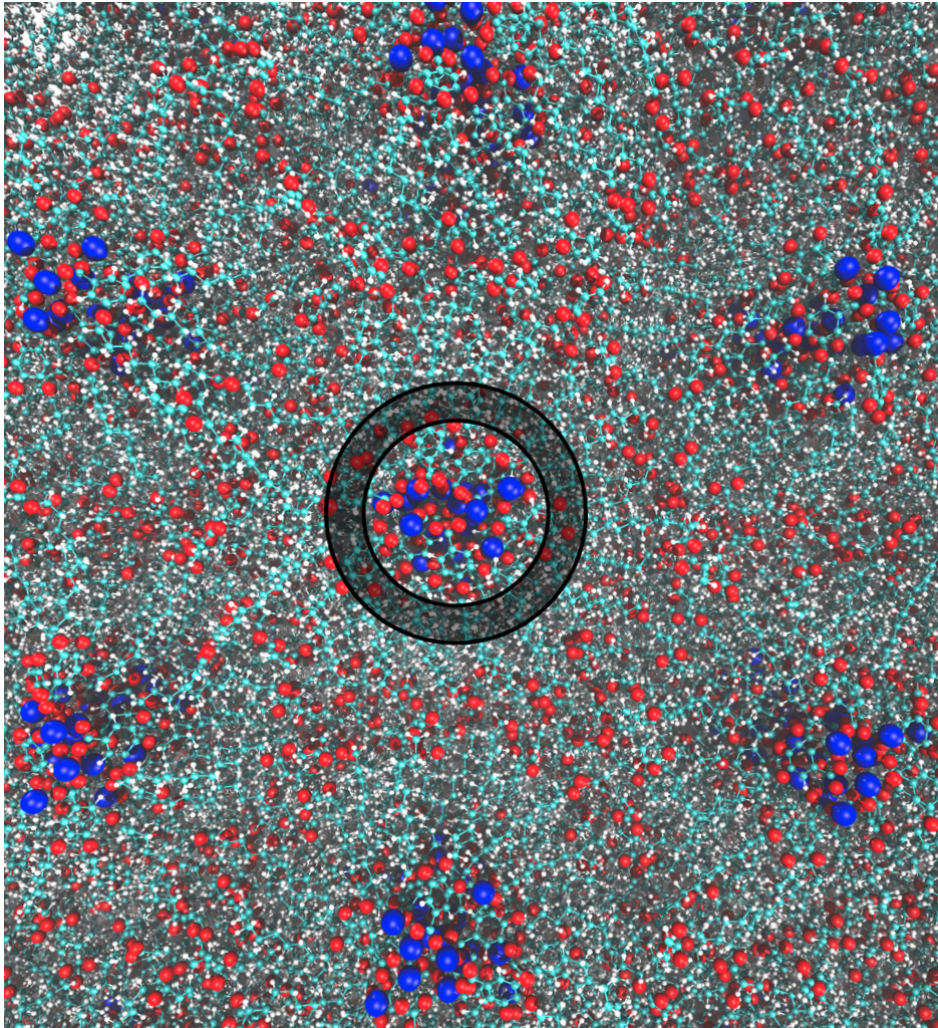


Figure 19: Looking down onto the plane of membrane, this diagram illustrates how we calculated radial distribution functions. We binned the radial distance of all atoms in chosen groups from pore centers. The pore centers are defined as the average coordinates of sodium ions in each pore. The bins are defined by the annulus bounded by concentric circles centered at the pore centers, as shown. To normalize, we divide the count of atoms within the bin annulus by the volume of the annulus where the volume is the area of the annulus times the height of the membrane in the z-direction.

simulated diffraction patterns of simplified configurations to understand why. We placed points in array that resemble the sandwiched and parallel displaced configurations. Points are space 3.7 \AA apart so it is easy to relate them to LLC membrane system. 5 columns of points are placed 5 \AA from a defined "pore center".

When points are stacked in either configuration, R-double cannot appear. In the case of

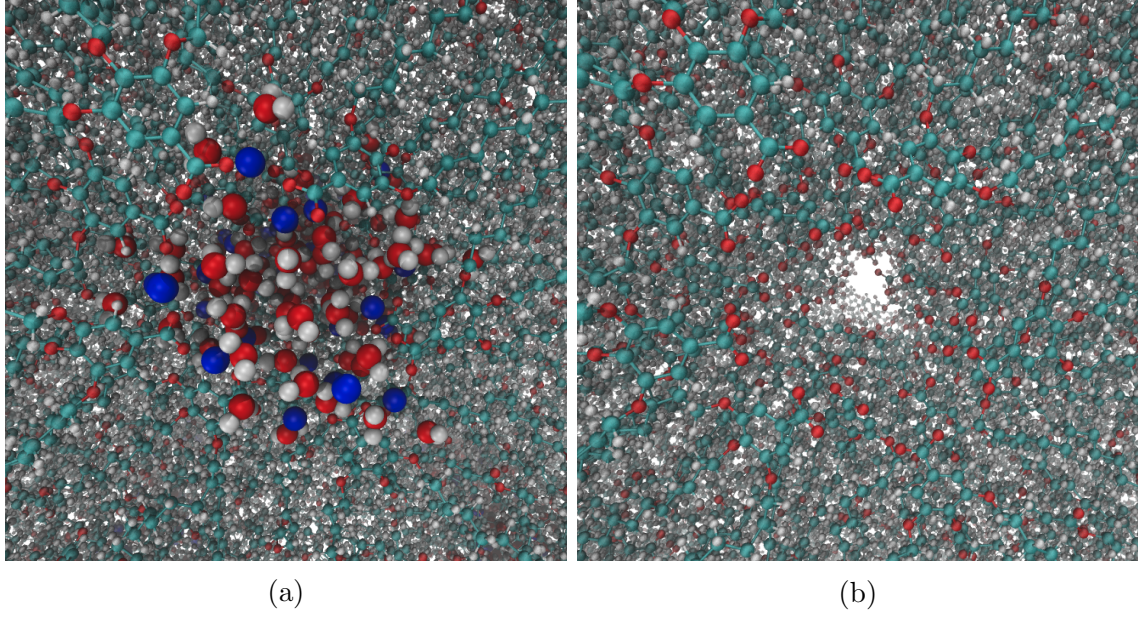


Figure 20: (a) Pores built in the parallel displaced configuration with 5 monomers per layer are filled with 5 wt% water. (b) The same system is visualized with water molecules and sodium ions removed. Head groups vacate the pore region leaving an aqueous solution of water and sodium ions.

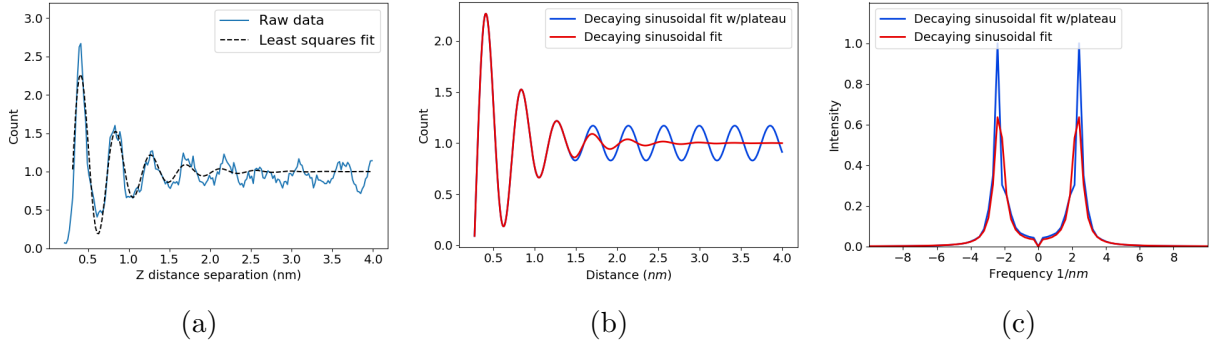


Figure 21: (a) We fit a decaying sinusoidal function to the z-correlation function, $g(z)$, calculated from the ordered basin sandwiched system. The oscillations in $g(z)$ continue to oscillate at nearly the same amplitude as its third peak. (b) We overlaid a plot of the fit to $g(z)$ with a similar function that continues to oscillate with the same amplitude as its third peak. (c) The power spectrum of each plot in (b) exhibits a 60 % increase in intensity of the peaks when the function does not decay to 1.

the sandwiched configuration, the fundamental frequency is set at 1.7 \AA^{-1} , the same location as $R-\pi$. Subharmonics appear at integer multiples of this frequency. The parallel displaced configuration exhibits reflections at half the q_z value of $R-\pi$, which is where we expect to see R-double. However, just like the LLC membrane system, the reflections appear away from

$q_r = 0$ and are caused by the helical stacking arrangement.

From these observations, it is clear that, in order to make R-double appear in our simulated diffraction patterns, we must create systems with asymmetries along the z-axis which lead to a fundamental frequency of 0.85\AA^{-1} . This requires a modulation in electron density every 7.4 \AA . This line of thought gave rise to the systems studied in section 3.2.3 of the main text.

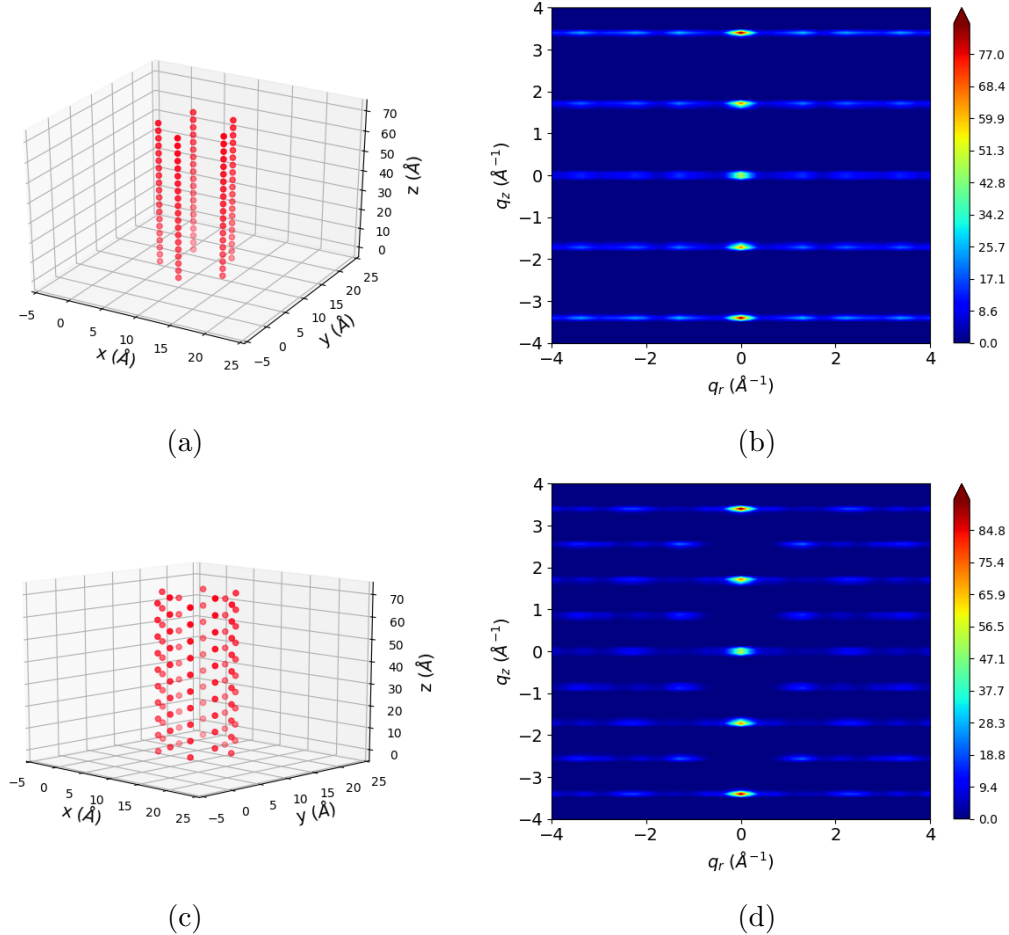


Figure 22

10 Crosslinking algorithm details

Crosslinking of the monomer Na-GA3C11 occurs by a UV initiated free radical polymerization (Figure 23). Head-to-tail addition takes place between terminal vinyl groups on

each of the monomer tails. We only considered head-to-tail addition since it is the dominant propagation mode in the real system.

Crosslink_mechanism-eps-converted-to.pdf

Figure 23: Terminal vinyl groups present on each monomer tail react with free radical initiators to create monomers with terminal vinyl radicals. Vinyl radicals react with the vinyl groups of other monomers in to propagate crosslinking.

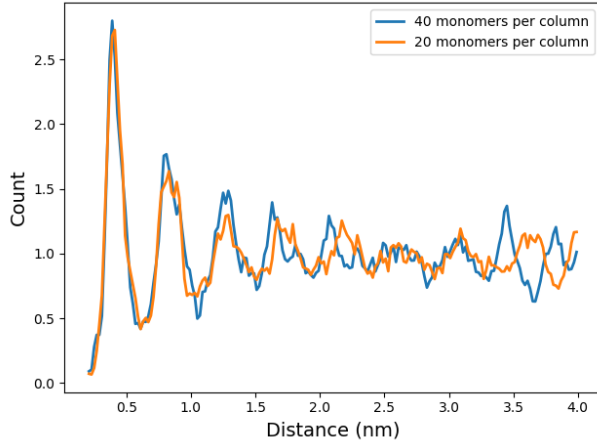


Figure 24: The correlation functions generated from ordered basin sandwiched configurations with different z-dimensions. The correlation function is nearly the same when the z-dimension of the system is doubled.

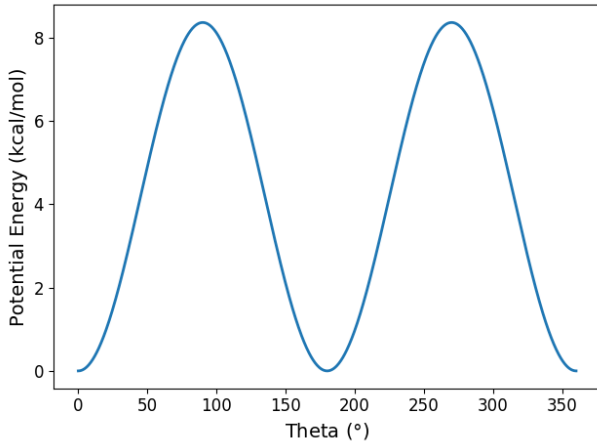


Figure 25: A potential energy diagram for the dihedral angle about the carbon-carbon bond of a carboxylate group attached to an aromatic ring, using parameters from the generalized amber forcefield. It is energetically favorable for the carboxylate group to stay in plane with the aromatic ring. There is a large energy penalty as the dihedral becomes antiparallel to the plane of the aromatic ring.

References

- () Martnez, L.; Andrade, R.; Birgin, E. G.; Martnez, J. M. PACKMOL: A package for building initial configurations for molecular dynamics simulations. *J. Comput. Chem.* **2009**, *30*, 2157–2164.
- () ChemAxon, MarvinSketch 17.13 2017 ChemAxon (<http://chemaxon.com>). 2017; <http://chemaxon.com>.
- () O’Boyle, N. M.; Banck, M.; James, C. A.; Morley, C.; Vandermeersch, T.; Hutchinson, G. R. Open Babel: An open chemical toolbox. *Journal of Cheminformatics* **2011**, *3*, 33.
- () The Open Babel Package, version 2.4.1 <http://openbabel.org>.
- () Wang, J.; Wang, W.; Kollman, P. A.; Case, D. A. Automatic atom type and bond type perception in molecular mechanical calculations. *Journal of Molecular Graphics and Modelling* **2006**, *25*, 247–260.
- () Case, D.; Betz, R.; Botello-Smith, W.; Cerutti, D.; Cheatham, T., III; Darden, T.; Duke, R.; Giese, T.; Gohlke, H.; Goetz, A. et al. AmberTools16. 2016.
- () Walker, R.; Tang, S. Antechamber Tutorial (ambermd.org/tutorials/basic/tutorial4b/).
- () Sousa da Silva, A. W.; Vranken, W. F. ACPYPE - AnteChamber PYthon Parser interface. *BMC Research Notes* **2012**, *5*, 367.
- () Chodera, J. D. A Simple Method for Automated Equilibration Detection in Molecular Simulations. *Journal of Chemical Theory and Computation* **2016**, *12*, 1799–1805.
- () Shirts, M. R.; Chodera, J. D. Statistically optimal analysis of samples from multiple equilibrium states. *The Journal of Chemical Physics* **2008**, *129*, 124105.